IOP PUBLISHING JOURNAL OF PHYSICS G: NUCLEAR AND PARTICLE PHYSICS

J. Phys. G: Nucl. Part. Phys. **39** (2012) 025201 (16pp) doi:10.1088/0954-3899/39/2/025201

Studies of the energy spectrum and composition of the primary cosmic rays at 100–1000 TeV from the GRAPES-3 experiment

H Tanaka[1], S R Dugad[1], S K Gupta[1], A Jain[1], P K Mohanty[1], B S Rao[1], K C Ravindran[1], K Sivaprasad[1], S C Tonwar[1], Y Hayashi[2], N Ito[2], S Kawakami[2], M Minamino[2], T Nonaka[2] and A Oshima[2]

[1] Tata Institute of Fundamental Research, Homi Bhabha Road, Mumbai 400 005, India
[2] Graduate School of Science, Osaka City University, Osaka 558-8585, Japan

E-mail: gupta@grapes.tifr.res.in

Received 25 September 2011
Published 12 January 2012
Online at stacks.iop.org/JPhysG/39/025201

Abstract

The composition and energy spectrum of primary cosmic rays (PCRs) are the only observables at high energies to study the nature of sources accelerating PCRs to $\geqslant$1000 TeV. These observables have been directly measured up to $\sim$300 TeV with detectors aboard balloons and satellites. But measurements at $>$1000 TeV have to be obtained indirectly from ground-based observations of extensive air showers. However, their interpretation relies on an inadequate knowledge of hadronic interactions at $\geqslant$1000 TeV. The GRAPES-3 experiment is designed to operate at $\geqslant$30 TeV providing a sizable overlap in energy with direct measurements, enabling the selection of a suitable model of hadronic interactions at $\sim$1000 TeV. We present salient features of GRAPES-3 including details of muon multiplicity distributions observed with a 560 m^2 detector as a function of shower size from an analysis of data of 545 days. These distributions were compared with expectations from Monte Carlo simulations, using some of the hadronic interaction generators in CORSIKA, to deduce energy spectra of five nuclear groups in the 100–1000 TeV region. A comparison of GRAPES-3 results with direct measurements indicates that SIBYLL provides a good description of hadronic interactions for interpreting our data. These measurements extend energy spectra and composition of PCRs that is consistent with extrapolation of direct measurements.

(Some figures may appear in colour only in the online journal)

1. Introduction

The energy spectrum of the primary cosmic rays (PCRs) is so remarkable that it can be described by a simple power law over nearly ten decades in energy, with only two changes

© 2012 IOP Publishing Ltd Printed in the UK & the USA

in the exponent at $\sim 3\times 10^{15}$ the *knee* and $\sim 3\times 10^{18}$ eV the *ankle*. Despite recent progress, an understanding of the nature of sources and acceleration mechanism(s) responsible for PCRs still eludes us. In the absence of direct detection of PCR sources, owing to their deflection in intervening the galactic magnetic field, precise measurements of energy spectra of different nuclear components over a wide energy range could be helpful in deciphering the process of their acceleration and propagation. At energies $\leqslant 300$ TeV, direct measurements from satellite and balloon platforms have provided crucial information on the composition and energy spectra of PCRs [1–4]. However, results obtained from direct measurements above 100 TeV suffer from limited statistics, due to relatively small exposures of $\leqslant 10^3$ m^2 h.

The indirect measurement on some of the components of an extensive air shower (EAS) such as electrons, muons, hadrons and Cherenkov photons from ground-based detectors is the only method available for study of PCRs, wherein exposure factors of $> 10^7$ m^2 h are achieved [5–12]. However, with the exception of Tibet-ASγ and ARGO-YBJ experiments [7, 8], the energy thresholds for most EAS arrays are significantly higher than the highest energy PCRs detected in direct experiments. This primarily is due to the large atmospheric overburden at observational sites, and also owing to practical constraints, such as large inter-detector separation in EAS arrays that contribute to higher threshold energies. Equally significant, the interpretation of the results from EAS observations are strongly influenced by the details of hadronic interaction generators used in simulations of EAS.

Due to the absence of data from accelerator experiments at $\geqslant 1000$ TeV in the laboratory frame, especially in the *forward* region relevant for propagation of an EAS in atmosphere, the details of assumptions made on the energy dependence of various interaction parameters have a major impact on the final outcome. In the past, different characteristics of an EAS, such as shower size (N_e), e-μ or e-h correlations, Cherenkov photon density, etc, were used to obtain the composition and energy spectrum at $\geqslant 1000$ TeV. Unfortunately, energy dependence of these components for different hadronic generators is often significantly different. Therefore, it is necessary to validate a combination of these observables along with a hadronic generator, by having a sizable overlap in energy with direct measurements. This objective was difficult to achieve for most of the EAS experiments, due to a variety of practical constraints, some of which have been outlined above.

Here, we report GRAPES-3 observations of muon multiplicity distributions (MMDs) [13–15] for several shower size 'N_e' groups that were used to obtain the energy spectra of various nuclear groups in PCRs in the range $\sim$100–1000 TeV. Therefore, a sizable overlap in energy $\sim$100–300 TeV of GRAPES-3 data with direct measurements could be achieved that helped in the selection of an appropriate hadronic generator. The well-known correlation between N_e and the muon content N_μ as a sensitive probe of PCR composition has been used in this work.

Simulations have shown that the shape of the MMD measured with a large area muon detector has excellent sensitivity to the composition of PCRs [10]. This is because lighter nuclei (H, He etc) predominantly contribute to lower multiplicities of MMD, as opposed to heavier nuclei (Al, Fe, etc) that dominate high multiplicities. This may be explained by considering two PCRs, an 'H' and an 'Fe', each having the same energy E_0. The Fe nuclei would break up in the first interaction producing A nucleons of energy $\sim E_0/A$ each, A is the mass number of Fe. In subsequent interactions, 'A' nucleons would produce a larger number of pions of systematically lower energy than those produced by H of same energy. The pions in Fe initiated EAS would more likely decay, producing a larger number of muons than in an H initiated EAS. These intuitive arguments are also supported by detailed simulations as shown subsequently.

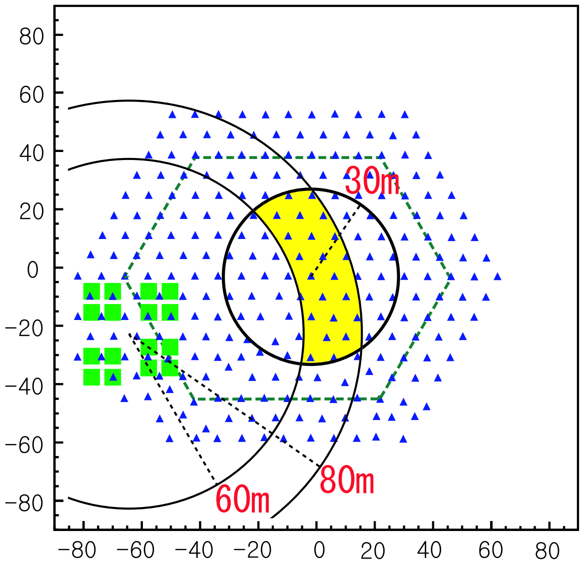

Figure 1. The GRAPES-3 experimental system of 257 scintillator detectors (▲) and 16 muon detector modules (🟩). Distances along the *X*- and *Y*-axes are in meters.

Salient features of the GRAPES-3 array are presented in section 2, details of the EAS trigger to optimize selection of lower energy EAS and muon detection efficiency are described in section 3 including the data analysis to obtain the EAS direction, size N_e, core location and MMDs for different-size group. In section 4, details of simulations are presented along with N_e and muon size distributions for three hadronic generators. Results obtained on energy spectra of H and other nuclear groups are compared with direct measurements in section 5. This is followed by a discussion on the suitability of different generators used in the energy range 100–1000 TeV in section 6. Conclusions are presented in the final section.

2. The GRAPES-3 experimental setup

The GRAPES-3 (Gamma Ray Astronomy at PeV Energies Phase-3) experiment consists of a densely packed EAS array at Ooty in India (11.4°N, 76.7°E, 2200 m). A schematic of the array of 257 scintillator detectors, each 1 m^2 and deployed on a hexagonal grid with the separation of 8 m [13], is shown in figure 1. Each detector is shown as a filled triangle. The hexagonal geometry in deployment of detectors ensured uniform selection of EAS, over the array.

The array also contains 16 modules of the tracking muon detector of total area 560 m^2 shown as filled squares in figure 1. A cluster of four modules is housed inside a common hall forming a supermodule. The hall contains signal processing and recording system for muons. Each 35 m^2 module consists of 232 proportional counters (PCs) deployed in four layers of 58 each, placed in orthogonal directions. This permits a reconstruction of muon track to an accuracy of 6° in two orthogonal vertical planes. Energy threshold of muons was $\sec(\theta)$ GeV, where θ is the muon angle relative to the vertical direction. An arrangement of concrete layers in the shape of an inverted pyramid provides the shielding up to 45° [14].

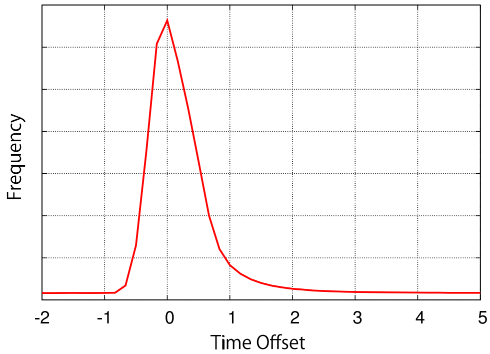

Figure 2. Muon time offset T_0 in μs.

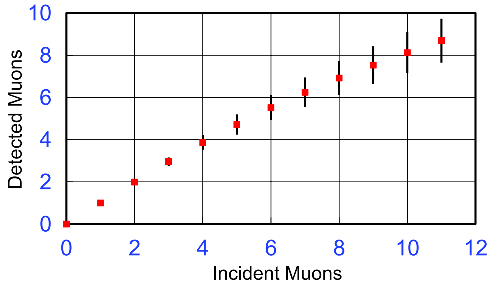

Figure 3. The number of reconstructed tracks as a function of incident muons from MC.

3. The trigger and data analysis

The 560 m^2 GRAPES-3 tracking muon detector was used to identify multiple muon tracks in each EAS. The muons due to accidental coincidences during the latency time of PCs, not associated with EAS, were rejected by recording the time offset 'T_0' of each muon relative to the EAS trigger. The distribution of T_0 for detected muons is shown in figure 2.

The peak in figure 2 is due to EAS muons, and the tail on both sides is due to the chance coincidence of unassociated muons. By limiting T_0 within −0.8–2.6 μs, the number of muons by chance was reduced to $\leqslant$0.2 per EAS. Since EAS muons are aligned along the EAS direction, a further reduction was achieved by reconstructing the muon direction in two orthogonal vertical planes ($X-Z$ and $Y-Z$, where Z is vertical) and by requiring tracks to be within 10° of the projected EAS direction. A number of muons were measured for each plane and the larger of the two was treated as the true muon number for that module. Total muons were obtained by summing all 16 modules. The twin criteria of restricting time offset and direction ensured a clean identification of EAS muons. This estimate is reliable for a small number of tracks, however, as the muon number increases, the tracks begin to overlap and their number is underestimated. This saturation effect in a 35 m^2 module was investigated through simulations and the results are displayed in figure 3.

For example, on average, ten incident muons actually get reconstructed as eight tracks. For 16 modules, this effect becomes significant for muon multiplicities of $\geqslant$120. But it is automatically accounted for, since the reconstruction capability of the detector was incorporated in EAS simulations. In analysis of real data, EAS cores landing between 60 and

80 m from the center of the muon detector were selected as shown in figure 1. This was not to reduce the saturation effect, but to minimize the probability of hadrons penetrating the muon detector.

The GRAPES-3 trigger is optimized to select low energy EAS, by requiring a 3-fold coincidence of detectors on three adjacent lines, formed by the inner 153 detectors located inside the dashed hexagon shown in figure 1. Also a minimum of $\geqslant$10 detectors must trigger, each with a signal of $\geqslant$30% of a minimum ionizing particle. The arrival time and charge in the photomultiplier (PMT) pulse was recorded for all detectors, to obtain direction (θ, ϕ) and size (N_e) [13]. CORSIKA simulations of the EAS [16] for five nuclei, H, He, N, Al and Fe, had shown a triggering efficiency of ~90% at 50 TeV for H that increases with mass, reaching 100 TeV for Fe [13]. For each trigger, the following information was recorded for each PC in the muon detector: (i) time of the digital pulse with a resolution of 167 ns, (ii) pulse width with a resolution of 333 ns. Due to the exponential shape of the amplified pulse, its width provides a measure of logarithm of the pulse amplitude.

Earlier simulations had shown that MMD is a sensitive probe of the relative mix of nuclei in PCRs [10]. The energy spectrum of five nuclei is extracted through a comparison of observed MMDs with simulation results for different generators of hadronic interactions. Lateral distribution is used to fit the EAS core, size N_e, age, etc. Errors in the core location, N_e and age were studied as a function of N_e. The dependence of the differential size spectrum with the zenith angle was also studied and used to derive the vertical flux.

6×10^8 EAS collected in a lifetime of 4.7×10^7 s (545 days), spread over 2 years, were analyzed to measure EAS parameters, including direction (θ, ϕ), size N_e, core x_c,y_c, age s. The zenith 'θ' and azimuth 'ϕ' were measured from timing data of each triggered detector. The angular resolution of the array is known using three methods, *even–odd*, *left–right* and shadow of the moon on the PCR flux. The angular resolution is 0.7° at $N_e \geqslant 10^4$ [18]. Here, EAS of $\theta < 25°$ and cores within 30 m from the array center as shown in figure 1 were used for analysis.

The EAS direction θ, ϕ was calculated by a χ^2 minimization of the relative arrival times of particles. N_e was obtained by fitting the Nishimura–Kamata–Greisen (NKG) lateral distribution function to observed densities [17]. Age (s) was calculated by the maximum likelihood algorithm MINUIT [26] as described below. If n_i particles pass detector i, located at (x_i, y_i), of area S_i, the expected density ρ_i was calculated as follows:

$$r_i = \sqrt{(x_i - x_c)^2 + (y_i - y_c)^2 - D^2} \tag{1}$$

$$D = (x_i - x_c)\sin\theta\cos\phi + (y_i - y_c)\sin\theta\sin\phi \tag{2}$$

$$\rho_i = C\left(\frac{r_i}{r_m}\right)^{s-2.0}\left(1 + \frac{r_i}{r_m}\right)^{s-4.5} \tag{3}$$

$$C = \frac{N_e}{2\pi r_m^2}\frac{\Gamma(4.5 - s)}{\Gamma(s)\Gamma(4.5 - 2s)} \tag{4}$$

where r_m is the Molière unit and $r_m = 103$ m for atmospheric depth at Ooty. For incident density ρ_i, the probability of detecting n_i particles is p_i, and then the probability of such detection is L, which may be derived from the following equations:

$$p_i = \frac{(\rho_i S_i\cos\theta)^{n_i}}{n_i!}e^{-\rho_i S_i\cos\theta} \tag{5}$$

$$L = \prod_i p_i. \tag{6}$$

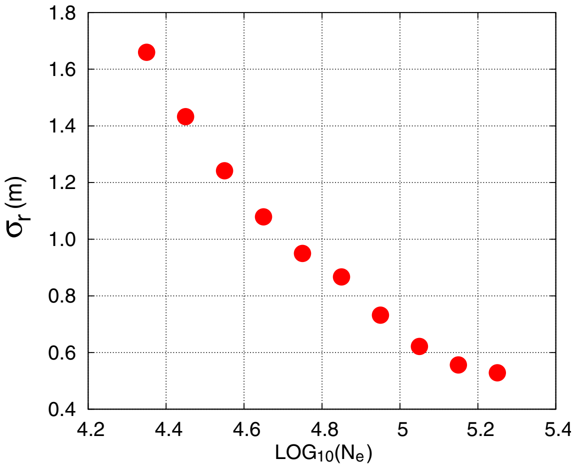

Figure 4. Mean error σ_r in the core location as a function of size N_e.

An increase in the path length for the zenith angle θ was included when estimating n_i. The unknown parameters were determined by maximizing the value of L. Since the detector response becomes nonlinear if the detected density $\rho_i S_i \sec(\theta)$ is $\geqslant$200, such detectors were excluded in the NKG fit. The detector i was rejected, if probability p_i was $\leqslant 10^{-4}$ of the expected value. MINUIT [26] was used for a successive approximation procedure to maximize L. The initial core position was estimated from the weighted mean of locations of seven detectors with the highest particle densities, labeled 'High7' where weights equaled density in the detectors. Approximations used in equation (8) were originally obtained from simulations:

$$\mathbf{R}_{\text{core}} = \frac{\sum_{\text{High7}} n_i \mathbf{r}_i}{\sum_{\text{High7}} n_i} \tag{7}$$

$$N_e = 102(n_i)^{0.97} \tag{8}$$

$$s = 1.0. \tag{9}$$

The core location accuracy was estimated by simulating proton EAS with the same reconstruction procedure as the real data. Next, the distance 'Δr' between the original and reconstructed cores was calculated. The mean of Δr termed mean error σ_r is shown with N_e in figure 4. The mean error σ_r improves with size, from ~1.6 m at $10^{4.3}$ to ~0.6 m at $10^{5.2}$. Similarly size accuracy was obtained by comparing $\mathrm{N_{fit}}$ from NKG with actual $\mathrm{N_{true}}$. For size range $10^{4.4} \leqslant N < 10^{5.2}$, rms errors were $\lesssim$10%. The mean of ratio $\mathrm{N_{fit}/N_{true}}$ is shown in figure 5 for 10 size groups, for the range $10^{4.3}$–$10^{5.3}$ in steps of $10^{0.1}$. Clearly, size is measured to ~8% at $N_e = 10^{4.4}$, and it improves to ~5% at $10^{5.2}$. However, the fitted size was always smaller than the true size when averaged over the size bin. Since the size for the measured and simulated EAS was being underestimated in exactly the same manner, it would not influence the final outcome on composition. A similar analysis for age 's' showed that an accuracy of ~0.1 was achieved.

Observed differential size (N_e) spectra for different zenith angles θ, grouped in bins of sec(θ) of width 0.05, are shown in figure 6. Flux values shown on the Y-axis were multiplied by ${N_e}^{2.5}$ for a clearer presentation. Statistical errors in data in figure 6 are very small, since each N_e, sec(θ) bin contains $>10^5$ EAS. A comparison of the nine spectra for sec(θ) from 1.025 (median of first bin) to 1.375 (for last bin) shows a close similarity, apart from differences in

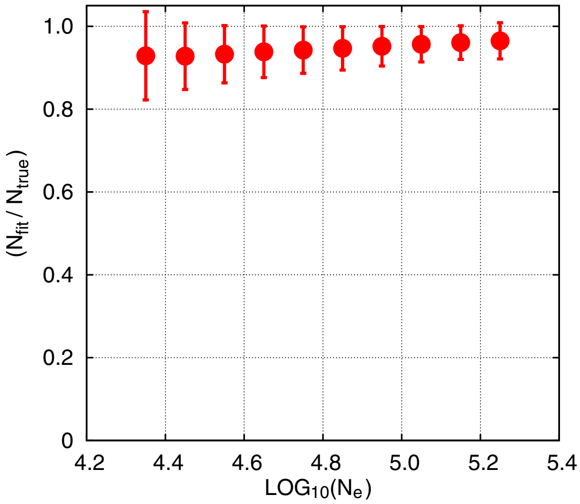

Figure 5. Ratio of ‘fitted’ and ‘true’ size from CORSIKA for 10 size groups. The *X*-axis is the logarithm of size.

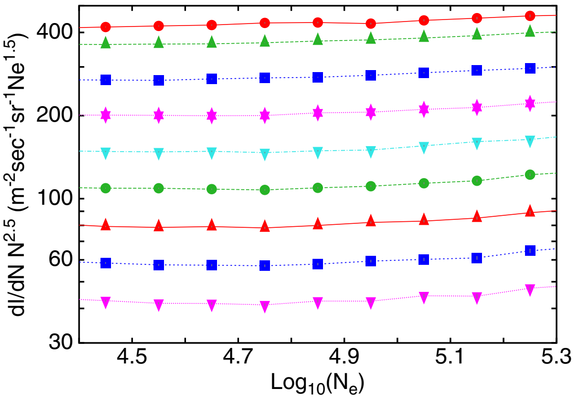

Figure 6. Observed N_e spectra for sec(θ) intervals of 0.05. Top plot ● vertical, second plot ▲ 1.00<sec(θ)<1.05, . . . , last plot ▼ 1.35<sec(θ)<1.40.

fluxes observed. Since the spectral slope is independent of θ, we combined the data for EAS with sec(θ) $< 25^\circ$, after suitable normalization, for further analysis of the muon content. The vertical flux shown in figure 6 derived from the EAS of $\theta < 25^\circ$ was converted into equivalent vertical size by following the relation, where vertical depth $X_v = 790$ g cm^{-2} and attenuation length $\lambda = 200$ g cm^{-2}:

$$N(0) = N(\theta)\,\mathrm{e}^{\frac{X_v}{\lambda}(\sec\theta - 1)}. \qquad (10)$$

Observed muons in 16 modules were counted by reconstruction of tracks based on hits in the four layers of PCs as described earlier. A muon outside the time window from −0.8 to 2.6 μs, relative to the EAS or if the direction was >10° from the EAS in any of the two planes was rejected as unassociated. EAS with cores between 60 and 80 m from the center of muon detector and inside a 30 m radius circle at the center of the array were selected. This kidney-shaped area of selection is shown as shaded in figure 1. The resultant MMD is shown in figure 9 for the size $10^{5.0} \leqslant N_e \leqslant 10^{5.2}$. Similar MMDs were obtained for the remaining sizes as shown in figure 6. MMDs were used for measuring energy spectra of five nuclei in PCRs. This was done by comparing observed MMDs with CORSIKA simulations after including the detector response from Geant4 [13] as discussed in the next section.

4. Monte Carlo simulations

Most ground-based experiments record electrons, muons, hadrons and other components deep down in the atmosphere ($\sim$8–10λ). Thus, detected particles at the observational level are the end product of hundreds of interactions at different depths in the atmosphere. Thus, the extraction of information on PCRs and characteristics of the first few ultra-high energy interactions require a comparison of observations with results with simulations, using generators of interactions for an assumed energy spectra of PCRs. Since the extreme forward region of interactions in the laboratory frame relevant here cannot be studied in high energy collider experiments, models of high energy interactions need to be extrapolated from energies of a TeV to 1000 TeV and beyond.

Since CORSIKA parameters to describe hadronic interactions are extrapolated from lower energy measurements, a significant model-dependent uncertainty in simulation results is to be expected. CORSIKA version 6.020 has several built-in hadronic generators [19]. The ones considered here include quark–gluon string-based QGSJet01 [20], dual parton with mini-jet based SIBYLL-2.1 [21], NEXUS-2.01 [22] generators, that hereafter would be referred to as QGSJet, SIBYLL, NEXUS, respectively. The low energy hadrons ($<$80 GeV) were treated using GHEISHA [23]. In CORSIKA, the electromagnetic cascade is treated by two methods, EGS4 code [24] or NKG function [17]. In EGS4, every particle is tracked but NKG calculates densities at the array level and runs faster than EGS4. To save computing time, we have used NKG. But we performed simulations using EGS4 for a limited number of events, to investigate differences between the two methods, after the folding detector response [13, 25]. Saturation effects on a number of muons at high multiplicities were accounted for. This comparison showed that final results were insensitive to the specific method used.

The PCRs were assumed to be of five species, protons (H, $A = 1$), helium (He, $A = 4$), nitrogen (N, $A = 14$), aluminum (Al, $A = 27$) and iron (Fe, $A = 56$). Heavier nuclei N, Al and Fe were used to represent light (CNO), medium (Mg, Al, Si) and heavy (Mn, Fe, Co) masses in PCRs. In simulations, PCR energies were randomly selected from a differential power law of slope -2.7 for the five nuclei. The selected threshold energies for H, He, N, Si, Fe were 5, 8, 16, 16, 20 TeV, respectively. The thresholds were sufficiently small, so that trigger efficiencies were $<10\%$ [13]. The core of each EAS was thrown randomly over an area of radius 100 m centered on the array. Each EAS was subjected to analysis identical to the one used for the observed EAS. Once the GRAPES-3 trigger criterion was met, then EAS parameters, N_e, N_μ etc were calculated to obtain simulated MMDs. Since MMDs for Al and Fe overlap substantially, they were combined by assuming a ratio of Al/Fe = 0.8 based on a direct experiment [3]. Since abundance ratio Al/Fe was fixed, effectively the number of independent species was reduced to 4. EAS with $\theta \leqslant 30^\circ$ were simulated, but only those with $\theta \leqslant 25^\circ$ were used in analysis. Muon and hadrons were tracked until their energy dropped below 1 GeV. Simulated MMDs for five nuclei were normalized per EAS and the fraction a_i of each nuclei was extracted by minimizing χ^2 using MINUIT to reproduce the observed MMD for each size N_e bin:

$$\chi^2 = \sum_k \frac{\left(n_{0k} - \sum_i a_i n_{ik}\right)^2}{\epsilon_{0k}^2 + \sum_i (a_i \epsilon_{ik})^2} \tag{11}$$

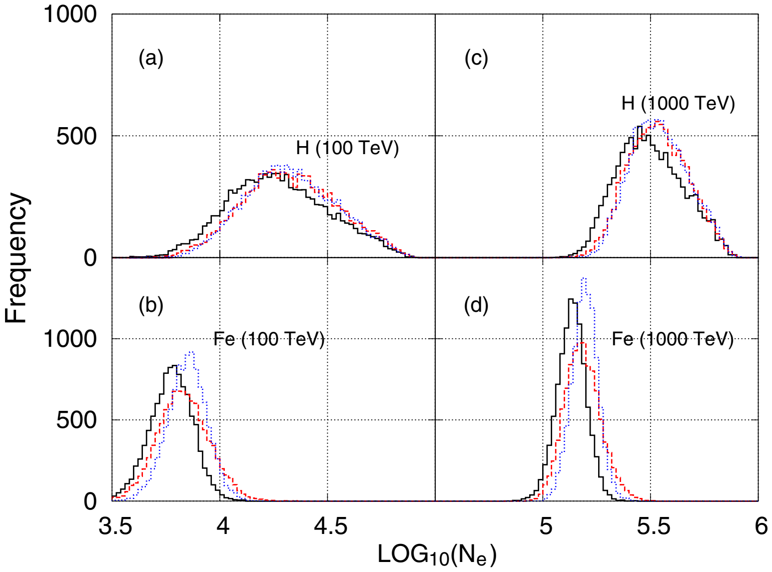

Figure 7. Size distribution at Ooty (790 g cm^{-2}, $\theta \leqslant 30^\circ$), (i) QGSJet continuous line, SIBYLL dashed line, NEXUS dotted line. Primary particle and energy: (a) H 100 TeV, (b) Fe 100 TeV, (c) H 1000 TeV, (d) Fe 1000 TeV.

where k is the multiplicity bin number, i the mass group, i.e. $i = 1{-}5$ for H, He, N, Al, Fe, respectively, and $i = 0$ is the observed data. n_{ik} and ϵ_{ik} are the mean frequency and statistical error for the kth bin. The initial value of parameter a_i was set to 0.2 and the effect of the initial value on the final result was found to be negligible.

It was pointed out by the CORSIKA team [16] that the fragmentation of the incident nucleus, from full fragmentation in the first interaction (superposition model) to partial fragmentation into other nuclei, led to essentially the same results for most observables deep down in the atmosphere, where EAS are observed. Any distinctive features of fragmentation are smeared out by fluctuations in the huge number of interactions, during development and propagation of EAS in the upper atmosphere. Therefore, we use a simpler superposition model and treat interactions of an incident nucleus of mass A, energy E as the superposition of A nucleons, each of energy 'E/A' from the first interaction.

Before a detailed comparison of observed MMDs for different N_e with simulations, it is useful to examine the broad features of predictions of different generators. Distributions of simulated N_e for H and Fe, for an energy of 100 TeV, are shown in figures 7(a) and (b) by continuous, dashed and dotted lines for QGSJet, SIBYLL and NEXUS, respectively. On average, QGSJet predicts a smaller N_e at Ooty compared to the other two generators. The ratio of N_e for H and Fe at 100 TeV is ~3. A similar result is obtained at 1000 TeV as seen in figures 7(c) and (d). Compared to QGSJet, N_e is ~10% larger for SIBYLL and is the largest for NEXUS. Comparison of N_e distributions at 100 and 1000 TeV shows a narrower one for Fe than H for all three generators. This behavior may be understood as follows: fluctuations in depth of the first interaction are smaller for Fe- than H-induced EAS due to superposition of a large number of cascades for Fe that reduces the fluctuations because of averaging.

A similar comparison of muons of energy > 1 GeV, the so-called muon size N_μ, in H and Fe EAS for the same generators, QGSJet, SIBYLL and NEXUS, is shown in figures 8(a) and (b) for 100 TeV and in figures 8(c) and (d) for 1000 TeV. N_μ on average is significantly larger

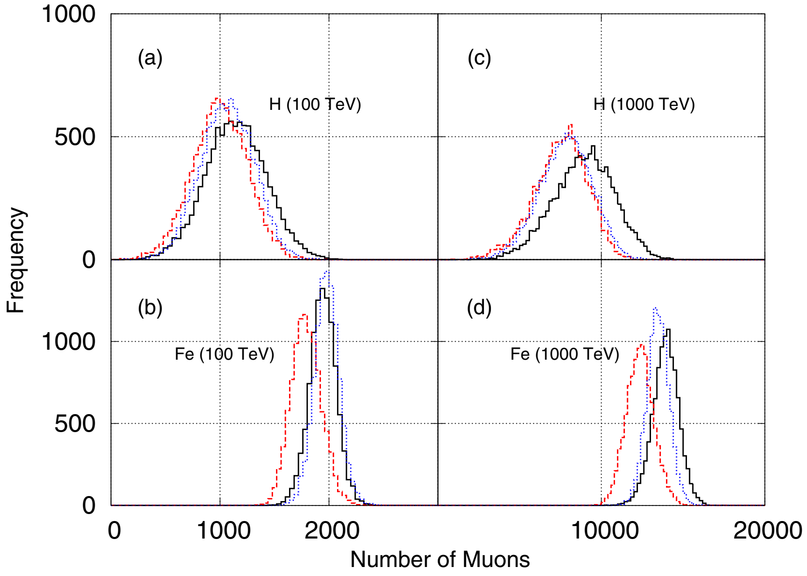

Figure 8. Distributions of $\geqslant$1 GeV muons at Ooty (790 g cm^{-2}, $\theta \leqslant 30^{\circ}$) for (i) QGSJet, continuous line, SIBYLL, dashed line, NEXUS, dotted line. Primary particle and energy: (a) H 100 TeV, (b) Fe 100 TeV (c) H 1000 TeV, (d) Fe 1000 TeV.

for QGSJet than SIBYLL or NEXUS. This reversal of trend further enhances the differences in MMDs when EAS of same N_e are compared, thus increasing the sensitivity of the MMD technique. At 100 TeV, muon distribution is significantly narrower for Fe- than H-induced EAS as shown in figures 8(a) and (b). The same trend is repeated at 1000 TeV as shown in figures 8(c) and (d), although this size-based selection does reduce the number of Fe EAS in the sample. In the next section, we compare experimental data with simulations using only QGSJet and SIBYLL since they were reported to provide better agreement with observational results [11, 27].

5. Results

GRAPES-3's objective is to compare indirect spectra with direct results. Thus, the number of simulated EAS were normalized to the number expected during the observed time of 4.71×10^{7} s. The detected EAS of a size N_e are more heavily dominated by H than Fe, as discussed in section 4 and shown in figure 7 and their ratio is ~3 for H and Fe at 100–1000 TeV. The observed MMD for N_e $10^{5.0}$–$10^{5.2}$ is shown as filled circles in figure 9(a). The error bars represent only statistical errors in data. Also shown are results of the simulated EAS initiated by H, He, N, Al and Fe using QGSJet. Relative abundances of four primary groups (Al/Fe ratio being fixed at 0.8) were obtained from a χ^2 minimization by fitting 4+1 simulated MMDs to the observed MMD displayed with error bars in figure 9(a). The summed distribution shown as the top histogram in figure 9(a) gives an excellent fit to the observed MMD for the full range of multiplicities from 0 to 60 muons. A comparison of the same observed MMD with the summed MMD for SIBYLL is shown in figure 9(b). This summed MMD also yields an equally good fit, although with different relative abundances of five nuclei.

A comparison of figure 9(a) and figure 9(b) shows that far fewer heavier nuclei are required to fit large ($n_\mu > 40$) multiplicities for QGSJet than SIBYLL. Smaller ($n_\mu < 10$)

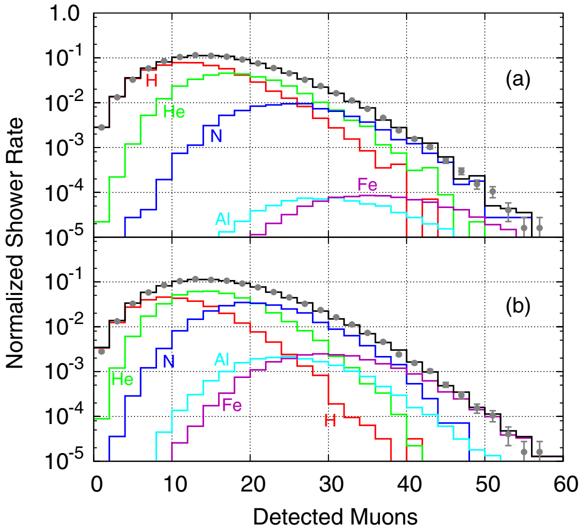

Figure 9. A comparison of the observed MMD for N_e $10^{5.0}$–$10^{5.2}$ with simulations for H, He, N, Al and Fe for (a) QGSJet, (b) SIBYLL. Note enhanced Al, Fe in SIBYLL.

multiplicities are entirely accounted for by lighter nuclei in both cases. The dominance of each mass group at different multiplicities underlies the sensitivity of this technique for the composition. Figures 9(a) and (b) also indicate evidence of heavier nuclei that generate the EAS in the $10^{5.0}$–$10^{5.2}$ region. This shows that interpretation of the same data requires significantly different compositions for the two generators. Similar behavior is seen for other sizes. Thus, the derived composition is intimately linked to the hadronic generator used. Since it was not possible to identify a unique hadronic generator from the GRAPES-3 data, we resorted to other constraints such as its consistency with direct results to identify the correct generator. Using the above procedure, relative abundances of four nuclei were obtained for QGSJet simulations for five sizes, $10^{4.2}$–$10^{4.4}$, $10^{4.4}$–$10^{4.6}$, $10^{4.6}$–$10^{4.8}$, $10^{4.8}$–$10^{5.0}$ and $10^{5.0}$–$10^{5.2}$. The variation in abundance of four nuclei for N_e $10^{4.2}$–$10^{5.2}$ is shown by filled squares in figure 10. Results for SIBYLL are shown by filled circles. Significantly different abundances for two generators are seen in figure 10.

The data show different trends for composition dependence of N_e. H is more abundant for QGSJet than SIBYLL, due to ~15% more muons in QGSJet than SIBYLL. This is reflected in the results shown in figure 10, where the H fraction for QGSJet is >70% at $N_e = 10^{4.3}$. Thereafter, the H fraction decreases with increasing N_e for both generators. The abundance of H sharply decreases by ~30% from $N_e = 10^{4.3}$–$10^{5.1}$ for both generators. This suggests a steeper spectra for H, than other nuclei. A fraction of He increases with N_e for QGSJet, but stays almost constant for SIBYLL. A different dependence is observed for the N fraction, that increases with N_e for SIBYLL, but is almost constant for QGSJet. The heavy fraction (Al+Fe) is much larger for SIBYLL than QGSJet. But a small fraction of ~5% (Al+Fe) at an N_e corresponds to a larger fraction ($\geqslant$15%) for the corresponding primary energy. This is because Fe-EAS develop faster, reach maximum N_e higher and then attenuate faster in lower atmosphere when detected. This leads to ~30% size of the H EAS for the same energy. However, the heavy fraction is much smaller at larger N_e for QGSJet. These results may have significant implications for the nature of the sources of PCRs and the acceleration processes dominating over the region 100–1000 TeV [28]. Next, observed N_e spectra were converted into

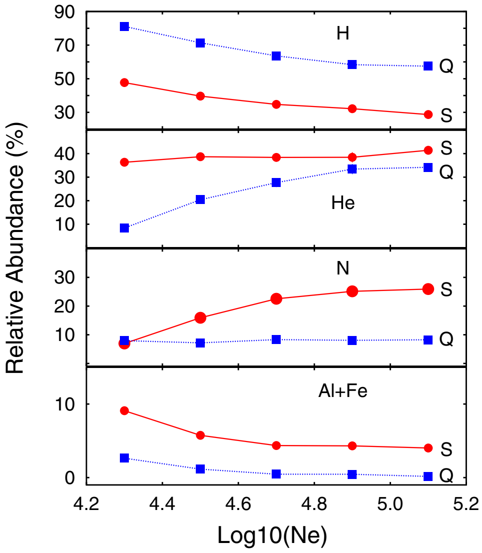

Figure 10. Relative abundance of four groups with N_e by ■ for QGSJet(Q) and by ● for SIBYLL(S).

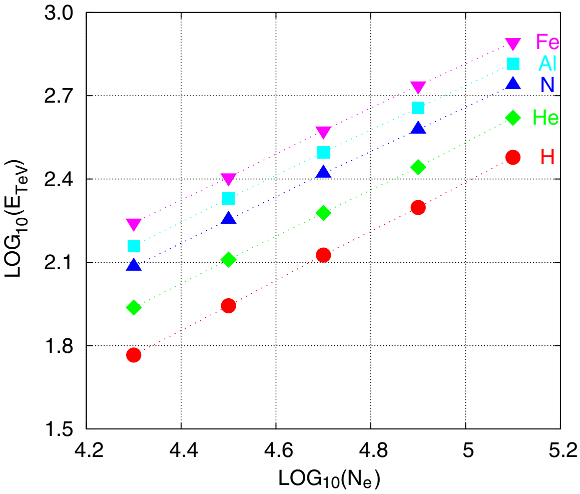

Figure 11. Size and energy relationship for five nuclei, (a) H ●, (b) He ◆, (c) N ▲, (d) Al ■, (e) Fe ▼ for SIBYLL. The dotted lines are there only to guide the eye.

energy spectra for five nuclei. Taking account of the exposure factor for data used in MMDs in figure 9 for a size and for the two generators, it is easy to convert relative abundances in figure 10 to fluxes for five nuclei at corresponding primary energy. The energy of each logarithmic N_e bin is computed from the logarithm of energy of the EAS in the bin, after imposing selection cuts discussed above.

An energy is assigned to each N_e, using size-to-energy relation from simulations for five nuclei and for two generators. The dependence of energy $\langle E_0 \rangle$ on $\langle N_e \rangle$ for five nuclei, namely H, He, N, Al, Fe for SIBYLL is shown in figure 11. The dotted lines joining data for individual nuclei are only to guide the eye. The ratio of energies of He and H at $N_e = 10^{4.3}$ is 1.5. Similarly

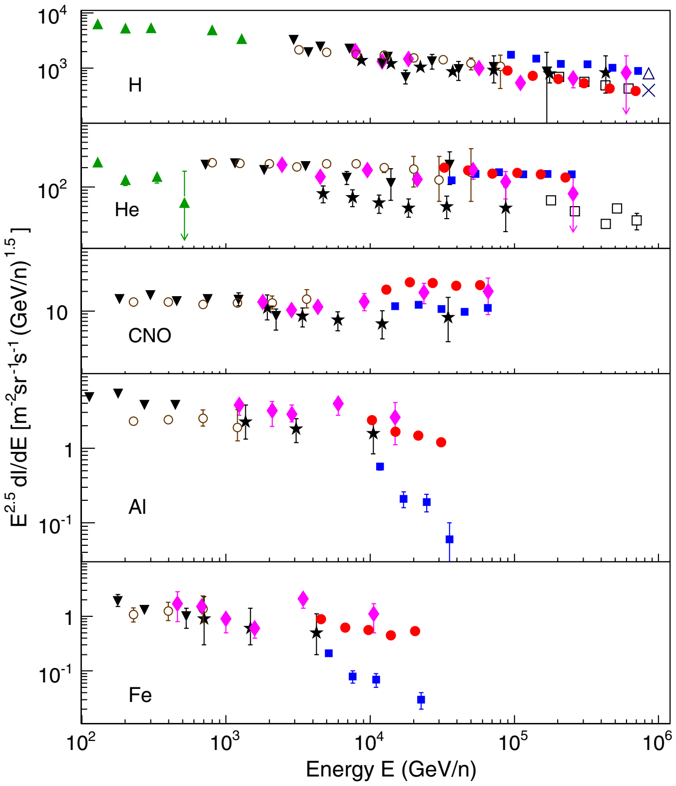

Figure 12. H, He, CNO, Al, Fe spectra from direct experiments: ▲ Ryan [29], ▼ SOKOL [30], ♦ JACEE [2], ★ RUNJOB [3], ○ CREAM [4], □ TIBET [7], KASCADE [11] × SIBYLL, △ QGSJet and GRAPES-3 ● SIBYLL, ■ QGSJET.

ratios for N, Al, Fe relative to H are 2.1, 2.5, 3.0, respectively, at $N_e = 10^{4.3}$. The magnitude of these ratios decreases slightly with increasing N$_e$, reducing by ~10% at $10^{5.1}$ as seen in figure 11. Next, N_e was converted into median energy using this relation. Energy spectra so derived for GRAPES-3 for H and He are shown in the top and second panel of figure 12 for QGSJet by filled squares and SIBYLL by filled circles. Spectra for N, Al, Fe are shown in the third, fourth and fifth panels in figure 12, respectively. These are compared with the results of the other groups: H and He data are from [2, 3, 29, 30] and N, Al and Fe are from [1, 3, 4, 30]. Also shown are results of indirect experiments, Tibet-ASγ on H, He [7] and KASCADE on H [11]. It may be recalled that GRAPES-3 spectra for Al and Fe are not independent since their relative abundance was fixed at 0.8, but are plotted separately for comparing them with direct results that are displayed in the five panels of figure 12.

A good agreement on composition and energy spectra of PCRs is seen between GRAPES-3 and direct results using SIBYLL, especially with JACEE, SOKOL and CREAM results [2, 30, 4]. This comparison shows that SIBYLL provides a better description of hadronic interactions in the overlap region of 100–300 TeV. Ours are absolute fluxes that were derived from N$_e$ and MMD directly, without recourse to any normalization. The extension of energy spectra by a factor of ~3 for five nuclei from GRAPES-3 is consistent with extrapolation from direct methods. Although N_e spectra shown in figure 6 can be fitted to a single power law, when combined with MMDs, different spectral slopes emerge for the 5 nuclei as seen

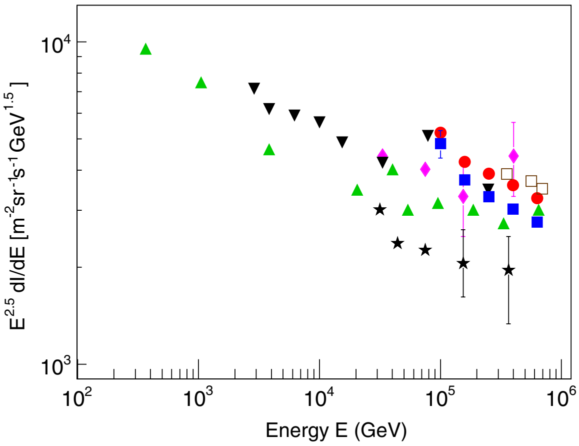

Figure 13. All-particle spectra from direct measurements: ▲ Grigorov [31], ▼ SOKOL [30], ♦ JACEE [2], ★ RUNJOB [3], and GRAPES-3 ● SIBYLL, ■ QGSJET, TIBET □.

in figure 12. The GRAPES-3 data are consistent with Tibet-ASγ in the overlap region of 200–700 TeV/n for H [7]. GRAPES-3 overlaps with KASCADE at 900 TeV and the H flux from KASCADE for SIBYLL and QGSJet [11] agrees closely with corresponding fluxes for GRAPES-3 as shown in figure 12. The consistency of our results using SIBYLL with direct methods underscores the utility of the energy overlap in the selection of a suitable generator. A comparison of the GRAPES-3 all-particle spectra with direct results [2, 3, 30, 31] shown in figure 13 also display good agreement, except for RUNJOB [3]. However, this comparison of all-particle spectra allows no distinction to be made between QGSJet and SIBYLL by the GRAPES-3 data.

6. Discussion

The analysis of 6×10^8 EAS and their muon content measured by GRAPES-3 is used to obtain MMDs as a function of N_e ($10^{4.2}$–$10^{5.2}$), corresponding to the energy range 100–1000 TeV. Simulated data in figure 7 show that for the same energy (100, 1000 TeV) H produces larger N_e EAS than Fe. Thus, if EAS are selected on N_e, then the sample contains H of ~3 times lower energy than Fe. For fixed energy (100, 1000 TeV), N_μ is a factor of ~2 larger for Fe than H as shown in figure 8. Thus, if EAS are binned in narrow N_e intervals and their MMDs examined, a muon multiplicity of approximately six times larger would be observed for Fe than H. However, this N_e based cut results in the selection of Fe of approximately three times higher energy and thus their fraction substantially reduces in the N_e bin, a limitation of this technique. However, even in the presence of a relatively small fraction of Fe, the MMD gets substantially enhanced at higher multiplicities. Such high multiplicities cannot be produced by lighter elements as shown in figure 9 for $10^{5.0} < N_e < 10^{5.2}$. This fact summarizes the sensitivity of GRAPES-3 to the mass composition of PCRs.

The above argument especially applies to the GRAPES-3 muon detector because (i) the identification of each muon is unambiguous, (ii) the muon statistics in an EAS are good due to the large area (560 m^2), (iii) the muon detector is compact, wherein the 560 m^2 detector is confined in a geographical area of ~1600 m^2. This allows the simulation of muons to be largely independent of details of the assumed shape of lateral distribution. As seen from figure 12, the abundances of Al and Fe are significantly lower for QGSJet than for SIBYLL. This difference is caused by the production of ∼15% more muons in QGSJet. Thus, QGSJet fits observed MMD even with a relatively lighter composition rather well as explained in section 5. It is to be reiterated that the derived composition is strongly dependent on the nature of assumed hadronic interactions. However, this is not a limitation unique to the GRAPES-3, but holds true for all EAS experiments. As our knowledge of hadronic interactions improves, especially with the start of the LHC, measurements of composition should also become progressively more precise.

A glance at figure 12 shows that predictions of both QGSJet and SIBYLL seem to agree with direct results for lighter nuclei within errors. However, a closer examination of GRAPES-3 data reveals that the flux of H with QGSJet is systematically higher by a factor of ∼2 than with SIBYLL. Despite the errors, the flux obtained using SIBYLL is much closer to the direct results than QGSJet and that is also true for the KASCADE flux at 900 TeV. This observation is especially relevant for comparison of H spectra for the following two important reasons: (i) fluxes from direct methods are intrinsically more reliable, especially at the lower end of the overlap energy region, and (ii) no major assumptions are needed for nuclear break-up in the first H air–nucleus collision.

QGSJet flux of CNO is systematically lower by a factor of ∼3 compared to SIBYLL. Here again SIBYLL is closer to more reliable direct results from JACEE and CREAM. Only in the case of He do both QGSJet and SIBYLL yield nearly the same fluxes consistent with the direct results. However, for heavier Al and Fe, the agreement with the direct results for SIBYLL is significantly better than QGSJet as seen in figure 12. In short, comparison of spectra for five nuclei obtained from MMDs with direct results shows the inadequacy of QGSJet to provide good agreement with data. But there is no significant difference in the spectra of He for both generators. However, differences between them widen for the three heavier nuclei.

Among the four direct experiments, JACEE, SOKOL, CREAM, RUNJOB, the GRAPES-3 results agree well with the first three experiments. But there is a discrepancy in fluxes of He reported by RUNJOB and JACEE/SOKOL/CREAM. GRAPES-3 results provide continuity to measurements from JACEE/SOKOL/CREAM. Another compelling inference from comparisons shown in figure 12 relates to the difference in steepness of the H spectrum relative to the other four nuclei that are decidedly flatter up to ∼1000 TeV. This difference in spectral slopes may have important implications for the nature of cosmic ray sources and the environment surrounding them in the range 100–1000 TeV within the galaxy. The GRAPES-3, H spectrum agrees well with the results of other indirect experiments, KASCADE [11] and Tibet AS/γ [7]. However, the He flux from Tibet AS/γ is in disagreement, with GRAPES-3 as well as JACEE, SOKOL and CREAM, probably showing the inadequacy of the N_e spectrum determined from an EAS array alone, to provide reliable spectral information on He and other heavier nuclei in PCRs.

7. Conclusions

The observations of MMDs with the large GRAPES-3 tracking muon detector have provided evidence of a steeper proton spectrum, consistent with direct measurements from balloon and satellite borne experiments. GRAPES-3 spectra for He, N, Al and Fe agree well with the direct results, extending the energy reach and confirming their flatter nature relative to protons. Our results indicate SIBYLL to be a suitable generator for describing hadronic interactions in the overlap energy region of 100–300 TeV. The extension of energy spectra by a factor of ∼3 up to ∼1000 TeV for five nuclei is consistent with the extrapolation of the spectra measured by direct methods. With greater confidence in the suitability of SIBYLL at these energies, analysis of larger size ($N_e > 10^{5.4}$) showers will be done for extending the measurements to the *knee* region and beyond, which may help in better understanding the physical process(es) responsible for this critically important feature in the energy spectrum of PCRs.

Acknowledgements

We thank D B Arjunan, G P Francis, I M Haroon, A Iyer, P Jagadeesan, V Jeyakumar, K Manjunath, S D Morris, S Murugapandian, B Rajesh, K Ramadass, C Ravindran, V Santhosh Kumar, R Suresh Kumar and V Viswanathan for their help in the installation and operation of GRAPES-3. This work is dedicated to the memory of our brilliant colleague S Karthikeyan who passed away in a tragic road accident.

References

[1] Kobayakawa K *et al* 2002 *Phys. Rev.* D **66** 083004
[2] Asakimori K *et al* 1998 *Astrophys. J.* **502** 278
Takahashi Y 1998 *Nucl. Phys.* B **60** 83
[3] Shibata T *et al* 2001 *Astropart. Phys.* **16** 13
Derbina V A *et al* 2005 *Astrophys. J. Lett.* **628** L41
[4] Ahn H S *et al* 2009 *Astrophys. J.* **707** 593
Ahn H S *et al* 2010 *Astrophys. J. Lett.* **714** L89
[5] Glasmacher M A K *et al* 1999 *Astropart. Phys.* **10** 291
[6] Aglietta M *et al* 1999 *Astropart. Phys.* **10** 1
[7] Amenomori M *et al* 2000 *Phys. Rev.* D **62** 112002
[8] Bacci C *et al* 2000 *Nucl. Instrum. Methods Phys. Res.* A **443** 342
[9] Fowler J W *et al* 2001 *Astropart. Phys.* **15** 49
[10] Gupta S K *et al* 2003 *Phys. Rev.* D **68** 052005
[11] Antoni T *et al* 2005 *Astropart. Phys.* **24** 1
[12] Chilingarian A *et al* 2007 *Astropart. Phys.* **28** 58
[13] Gupta S K *et al* 2005 *Nucl. Instrum. Methods Phys. Res.* A **540** 311
[14] Hayashi Y *et al* 2005 *Nucl. Instrum. Methods Phys. Res.* A **545** 643
[15] Hayashi Y 2005 *Proc. 29th Int. Cosmic Ray Conf. (Pune)* vol 10 p 243
[16] Heck D *et al* 1998 *Report FZKA* 6019 Forschungszentrum Karlsruhe
[17] Greisen K 1960 *Annu. Rev. Nucl. Sci.* **10** 63
Kamata K *et al* 1958 *Suppl. Prog. Theor. Phys.* **6** 93
[18] Oshima A *et al* 2010 *Astropart. Phys.* **33** 97
[19] Knapp J *et al* 1996 *Report FZKA* 5828 Forschungszentrum Karlsruhe
Heck D *et al* 2001 *Proc. 27th Int. Cosmic Ray Conf. (Hamburg)* vol 1 p 233
[20] Kalmykov N N *et al* 1997 *Nucl. Phys.* B **52** 17
[21] Fletcher R S *et al* 1994 *Phys. Rev.* D **50** 5710
Engel R *et al* 1999 *Proc. 26th Int. Cosmic Ray Conf. (Salt Lake City)* vol 1, p 415
[22] Drescher H J *et al* 2001 *Phys. Rep.* **350** 93
[23] Fesefeldt H 1985 *Report PITHA-85/02* RWTH Aachen
[24] Bielajew A F *et al* 1994 *National Research Council Canada Report* NRC-PIRS-0436
[25] Yoshikoshi T *et al* 2001 *Proc. 27th Int. Cosmic Ray Conf. (Hamburg)* vol 2 p 612
[26] James F 1998 *MINUIT CERN Prog.* Library D506
[27] Milke J *et al* 2004 *Acta Phys. Polon.* B **35** 341
[28] Meli A and Biermann P L 2006 *Astron. Astrophys.* **454** 687
[29] Ryan M J *et al* 1972 *Phys. Rev. Lett.* **28** 985
[30] Ivanenko I P *et al* 1993 *Proc. 23rd Int. Cosmic Ray Conf. (Calgary)* vol 2 p 17
[31] Grigorov N L *et al* 1971 *Proc. 12th Int. Cosmic Ray Conf. (Hobart)* vol 5 p 1746